






Diffusiophoresis and diffusioosmosis in tandem: Two-dimensional particle motion in the presence of multiple electrolytes

Benjamin M. Alessio ¹, Suin Shim ², Emmanuel Mintah ³,
Ankur Gupta ^{2,4} and Howard A. Stone ²

¹*Department of Physics, Princeton University, Princeton, New Jersey 08544, USA*

²*Department of Mechanical and Aerospace Engineering, Princeton University, Princeton, New Jersey 08544, USA*

³*Department of Chemical and Biological Engineering, Princeton University, Princeton, New Jersey 08544, USA*

⁴*Department of Chemical and Biological Engineering, University of Colorado, Boulder, Colorado 80301, USA*



(Received 16 December 2020; accepted 20 April 2021; published 13 May 2021)

Diffusiophoresis is the movement of colloidal particles due to a gradient in the concentration of a solute. Previous studies on diffusiophoresis have focused largely on one-dimensional colloid transport due to the gradient of a single electrolyte. Recent studies have considered two-dimensional geometries including dead-end pores, multiple electrolytes, and a background flow field due to diffusioosmosis. In this work, we develop a model of the time-dependent diffusiophoretic compaction of colloids in a two-dimensional pore due to the gradient of multiple electrolytes in tandem with a diffusioosmotic slip-driven background flow field, which builds upon these recent studies by combining each of these effects. We simulate this model for varying properties of the pore walls and colloidal particles. Furthermore, we conduct experiments varying the initial ion combinations and total solute concentration, which show good qualitative agreement with the simulations. Our results indicate that diffusiophoretic compaction can be increased or decreased by manipulating electrolyte combinations, total solute concentration, wall charge, and particle diffusivity; each effect can modify the particle velocity, with varying strength, in unison or in opposition to the other effects. By offering a larger toolbox to manipulate colloidal particles, our results on diffusiophoretic and diffusioosmotic motion in tandem and in the presence of multiple electrolytes can be exploited for lab-on-a-chip and biophysics applications.

DOI: [10.1103/PhysRevFluids.6.054201](https://doi.org/10.1103/PhysRevFluids.6.054201)

I. INTRODUCTION

Diffusiophoresis refers to the spontaneous motion, typically 1–10 $\mu\text{m/s}$, of colloidal particles driven by a gradient in solute concentration. It was discovered for nonelectrolytes by Derjaguin *et al.* [1] and for electrolytes by Dukhin *et al.* [2]. For electrolyte solutions, concentration gradients of cations and anions with different diffusivities set up a local electric field, generating a nonzero electrophoretic contribution to the diffusiophoretic velocity of charged particles [3]. The concentration gradient of solutes also produces a local gradient in osmotic pressure near the surface of the particles, causing chemiphoretic migration. Typically, observations of diffusiophoresis occur because of a combination of these two contributions. Many theoretical and experimental studies of diffusiophoresis focused on valence-symmetric solutes in two-ion electrolytes (e.g., LiCl, NaCl, KCl, etc.) [3–15]. For these systems, in the thin double-layer approximation, the electrophoretic

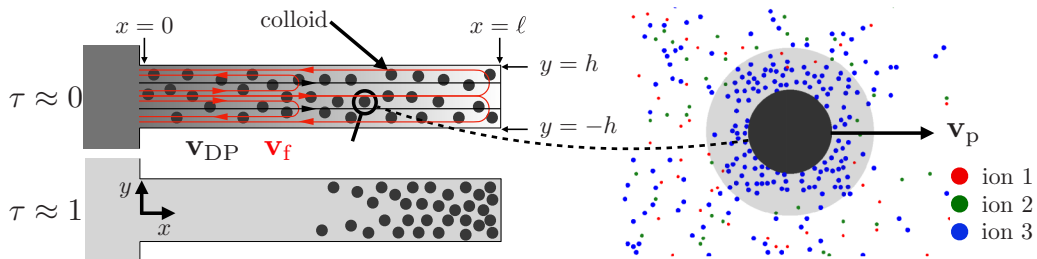


FIG. 1. Schematic of the transport of colloidal particles inside a pore in the presence of a three-ion solute concentration gradient. An example of a microscopic view of a single colloidal particle is shown to the right. The ion concentration gradients induce a diffusioosmotic slip velocity, which generates a flow field \mathbf{v}_f in the solution, as well as a diffusiophoretic velocity \mathbf{v}_{DP} on the particles. The net velocity of the particles $\mathbf{v}_p = \mathbf{v}_{DP} + \mathbf{v}_f$ is a superposition of diffusiophoretic and fluid velocities. The pore at $\tau \approx 0$ shows the initial state of the colloidal particles in a nonzero solute gradient, and the pore at $\tau \approx 1$ shows the colloidal particles in a compacted state after the ions have diffused throughout the length of the pore.

contribution is proportional to the diffusivity difference factor $\beta = (D_+ - D_-)/(D_+ + D_-)$, where D_+ and D_- denote, respectively, the diffusivities of the cation and anion.

Many recent studies consider diffusiophoresis in a dead-end pore configuration, which effectively creates (an approximate) one-dimensional transport of colloids and solutes under a controlled concentration gradient [13,16–21]. In such a geometry, the observation of particle migration is achieved by either tracking a peak location of the distribution, or measuring the extent of compaction of particles into the pores. Since the channel walls are also charged surfaces, diffusioosmotic flow of the aqueous phase is created along the pore walls. This slip velocity generates a nonuniform flow of liquid in the pores to maintain the continuity (zero net flux of the bulk liquid) [16,17]. Therefore, the advective particle motion that is observed in the pores is a combination of diffusiophoresis and the local flow velocity induced by the diffusioosmotic wall slip.

In this article, we investigate the motion of polystyrene (PS) particles in a dead-end pore geometry, and analyze using numerical simulations the two-dimensional motion under the influence of multiple electrolytes. Several recent studies employed multi-ion configurations [22–24], showing spontaneous migration of colloids in the concentration gradient. However, the reports do not provide a systematic understanding of the effect of multiple ions or varying the surface potential [13] of the experimental materials, nor do they account for the two-dimensional contribution of the diffusioosmotic wall slip. We present theoretical models and experiments for compaction of colloids in a pore with charged walls and multiple solutes. The two-dimensional numerical simulations, which consider varying surface potential, varying particle diffusivity, and the presence of three ions (Na^+ , K^+ , and Cl^-) in the solution, are compared with experimental measurements.

II. MATHEMATICAL MODEL

We consider a two-dimensional pore geometry shown in Fig. 1, where x spans $0 \rightarrow \ell$ and y spans $-h \rightarrow h$, such that $h \ll \ell$. The pore is connected to a main channel that acts as a reservoir. We assume that the pore is initially filled with an electrolyte solution containing sparse colloidal particles. To induce a diffusiophoretic motion, an ion concentration gradient is set up by flowing a different electrolyte solution in the main channel. The concentration gradient evolves with time and the colloidal particles subsequently compact through diffusiophoresis; see Fig. 1. The solutions consist of two electrolytes, NaCl and KCl, and their concentrations are varied in the pore as well as the main channel to investigate the effect of multiple electrolytes on diffusiophoresis and diffusioosmosis. For simplicity, we assume that the finite Debye length effects are negligible (see Ref. [13] for more details). To model the diffusiophoretic process, we solve for the concentrations

of electrolytes undergoing advective diffusion (described in Sec. II A) and of colloids undergoing diffusiophoresis in response to the electrolyte diffusion (described in Sec. II B). Although individual elements of these kinds of experiments and simulations have been reported previously, this report integrates all of the elements into one study. We note that we do not utilize a three-dimensional model since the differences between two- and three-dimensional predictions are relatively minor [25].

A. Transport of multiple solutes

Since NaCl and KCl share a common anion, we describe the concentrations C_i and diffusivities D_i of the three ions in the electrolyte solution as Na^+ ($i = 1$), Cl^- ($i = 2$), and K^+ ($i = 3$). To nondimensionalize the equations, we define $c_i = C_i/C_0$, $X = x/\ell$, $Y = y/\ell$, $\tau = tD_1/\ell^2$, $\mathcal{D}_i = D_i/D_1$, and $\mathbf{V} = \mathbf{v}\ell/D_1$ (for all velocities), where C_0 is a characteristic concentration, ℓ is the length of the pore, and $D_1 = 1.33 \times 10^{-9} \text{ m}^2/\text{s}$ is the diffusivity of Na^+ in water [26].

The Nernst-Planck equation relates the concentration of the i th ion to its flux and a background fluid velocity field according to [27]

$$\frac{\partial c_i}{\partial \tau} = -\nabla \cdot (\mathbf{J}_i + \mathbf{V}_f c_i), \quad (1)$$

where $\nabla = (\partial/\partial X)\hat{\mathbf{e}}_X + (\partial/\partial Y)\hat{\mathbf{e}}_Y$ and \mathbf{V}_f is the nondimensional fluid velocity. The nondimensional flux $\mathbf{J} = \mathbf{j}\ell/(D_1 C_0)$ is given by

$$\mathbf{J}_i = -\mathcal{D}_i(\nabla c_i + z_i c_i \nabla \Psi), \quad (2)$$

where the nondimensional electric potential is $\Psi = e\psi/(k_B T)$ and z_i is the valence of the i th ion. We invoke that the solution is electrically neutral and has zero electric current, which can be expressed by the following two equations:

$$\sum_{i=1}^3 z_i c_i = 0 \quad (3)$$

and

$$\sum_{i=1}^3 z_i \mathbf{J}_i = \mathbf{0}. \quad (4)$$

Combining Eqs. (2) and (4) yields the form of the gradient of the electric potential:

$$\nabla \Psi = -\frac{\sum_{i=1}^3 z_i \mathcal{D}_i \nabla c_i}{\sum_{i=1}^3 z_i^2 \mathcal{D}_i c_i}. \quad (5)$$

Furthermore, the background fluid velocity \mathbf{V}_f arises in our system from the diffusioosmotic wall slip with velocity [28] $\mathbf{V}_s = V_s \hat{\mathbf{e}}_X$, i.e., only in the direction parallel to the pore walls. The dimensional slip velocity $v_s = \varepsilon k_B^2 T^2 / (e^2 \mu D_1) f(\Psi_w, D_i, \nabla c_{iw})$, where $\varepsilon = 6.8 \times 10^{-10} \text{ F/m}$ is the electrical permittivity of the solution, $k_B = 1.38 \times 10^{-23} \text{ J/K}$ is the Boltzmann constant, $T = 298 \text{ K}$ is the absolute temperature, $e = 1.6 \times 10^{-19} \text{ C}$ is the elementary charge, and $\mu = 1.0 \times 10^{-3} \text{ Pa s}$ is the solution viscosity (assumed constant). Therefore, $V_s = \alpha f(\Psi_w, D_i, \nabla c_{iw})$, where we define

$$\alpha \equiv \frac{\varepsilon k_B^2 T^2}{e^2 \mu D_1}. \quad (6)$$

We adopt the approximate form [29] for $f(\Psi_w, D_i, \nabla c_{iw})$ to write

$$V_s = -\alpha \left(\frac{\sum_{i=1}^3 z_i \mathcal{D}_i \frac{\partial c_{iw}}{\partial X}}{\sum_{i=1}^3 z_i^2 \mathcal{D}_i c_{iw}} \Psi_w + \frac{1}{8} \frac{\sum_{i=1}^3 z_i^2 \frac{\partial^2 c_{iw}}{\partial X^2}}{\sum_{i=1}^3 z_i^2 c_{iw}} \Psi_w^2 \right), \quad (7)$$

where Ψ_w is the zeta potential of the wall and c_{iw} is the concentration of the i th ion at the wall. We note that while the expression in Eq. (7) is only valid for $|\Psi_w| \ll 1$, it can be utilized for moderate zeta potentials with reasonable accuracy [29].

We consider the pore wall to have a constant surface charge, which requires that its zeta potential depends on concentration, i.e., $\Psi_w = \Psi_w(c_{iw}(X, \tau))$ for $i = 1, 2$, and 3. We note that polymeric surfaces are most accurately represented by a charge regulation boundary condition [30]. However, such a boundary condition needs additional parameters and thus we invoke the constant charge boundary condition, which is reasonable for polystyrene particles and polydimethylsiloxane (PDMS) walls, as our previous study [13] demonstrates for a wide range of NaCl concentrations. Because we assume a constant surface charge, the following condition holds [29]:

$$\sum_{i=1}^3 c_{iw} [\exp(-z_i \Psi_w) - 1] = \text{constant}. \quad (8)$$

In the thin double-layer limit, the background fluid velocity field is determined by the Stokes equation [31]

$$\nabla^2 \mathbf{V}_f = \nabla P, \quad (9)$$

where P is the nondimensional pressure acting on the fluid. The narrow pore geometry ($\ell \gg h$) allows us to neglect the pressure gradient in the Y direction, as is common in the lubrication approximation. To acquire the X direction pressure gradient, we assume there is zero volumetric flux through a cross section of the pore. This gives an expression for the X -direction fluid velocity [25]:

$$V_{fX} = \frac{V_s}{2} \left[3 \left(\frac{Y}{h/\ell} \right)^2 - 1 \right]. \quad (10)$$

Since $\mathbf{V}_s = V_s \hat{\mathbf{e}}_X$, the incompressibility condition $\nabla \cdot \mathbf{V}_f = 0$ then yields an expression for the Y -direction fluid velocity:

$$V_{fY} = -\frac{Y}{2} \frac{\partial V_s}{\partial X} \left[\left(\frac{Y}{h/\ell} \right)^2 - 1 \right]. \quad (11)$$

Equation (10) indicates that $V_{fX} = V_s$ at the walls ($Y = \pm h/\ell$) and $V_{fX} = -V_s/2$ at the center line ($Y = 0$). Therefore, the axial fluid velocity changes sign to ensure zero flow rate through a cross section of the pore.

B. Transport of colloidal particles

Next, we consider the transport of a dilute suspension of colloidal particles due to the advective diffusion of multiple solutes described in Sec. II A. Similarly to Eq. (1), we describe the transport of the particles with nondimensional concentration $n = N/N_0$, for a given initial concentration N_0 , by

$$\frac{\partial n}{\partial \tau} = \nabla \cdot (\mathcal{D}_p \nabla n - \mathbf{V}_p n). \quad (12)$$

The nondimensional particle diffusivity is $\mathcal{D}_p = D_p/D_1$ and the nondimensional colloidal particle velocity is \mathbf{V}_p . We assume that the particles move relative to the fluid owing to diffusiophoretic transport, so that the particle velocity can be written

$$\mathbf{V}_p = \mathbf{V}_{DP} + \mathbf{V}_f. \quad (13)$$

We know the fluid velocity from Eqs. (7), (10), and (11). The diffusiophoretic velocity can be evaluated as [29]

$$\mathbf{V}_{\text{DP}} = \alpha \left(\frac{\sum_{i=1}^3 z_i \mathcal{D}_i \nabla c_i}{\sum_{i=1}^3 z_i^2 \mathcal{D}_i c_i} \Psi_p + \frac{1}{8} \frac{\sum_{i=1}^3 z_i^2 \nabla c_i}{\sum_{i=1}^3 z_i^2 c_i} \Psi_p^2 \right), \quad (14)$$

where Ψ_p is the zeta potential of the particle and α remains the same as in Sec. II A. Equation (14) is equivalent to the diffusioosmotic velocity given by Eq. (7) after transforming to the reference frame of the particle and replacing c_{iw} with c_i . We solve for Ψ_p by adjusting Eq. (8) to the case of a colloidal particle with constant surface charge according to

$$\sum_{i=1}^3 c_i [\exp(-z_i \Psi_p) - 1] = \text{constant}. \quad (15)$$

Equations (1) and (12) are therefore coupled by Eq. (13). A full solution for $n(X, Y, \tau)$ along with $c_i(X, Y, \tau)$ can be obtained numerically for given boundary conditions.

III. COMPUTATIONAL SYSTEM

We implemented a numerical PDE solver for the coupled Eqs. (1) and (12). The solver is implemented in MATLAB (ver. 2017b) [32] based on an implicit finite-volume scheme. To determine $\Psi_w(c_{iw})$ from Eq. (8), we introduce parameters Ψ_w^* and c_{iw}^* . Therefore, constant surface charge can be described as

$$\sum_{i=1}^3 c_{iw} [\exp(-z_i \Psi_w) - 1] = \sum_{i=1}^3 c_{iw}^* [\exp(-z_i \Psi_w^*) - 1], \quad (16)$$

where by changing Ψ_w^* and c_{iw}^* , we can represent different wall properties. Similarly, to obtain $\Psi_p(c_{ip})$ from (15), we introduce Ψ_p^* and c_i^* such that

$$\sum_{i=1}^3 c_i [\exp(-z_i \Psi_p) - 1] = \sum_{i=1}^3 c_i^* [\exp(-z_i \Psi_p^*) - 1]. \quad (17)$$

We summarize all the parameters and their values used for our computations in Table I.

A. Computing solute concentrations

We consider the case of a solution initially containing only KCl outside of the pore with a solution containing only NaCl inside the pore; the concentrations are chosen to be equal. Our solver first calculates the solute concentrations c_1 , c_2 , and c_3 . We take as initial conditions

$$c_1(X, Y, \tau = 0) = 1, \quad c_2(X, Y, \tau = 0) = 1, \quad c_3(X, Y, \tau = 0) = 0, \quad (18)$$

and boundary conditions

$$c_1(X = 0, Y, \tau) = 0, \quad c_2(X = 0, Y, \tau) = 1, \quad c_3(X = 0, Y, \tau) = 1, \quad (19)$$

$$\frac{\partial c_i}{\partial X}(X = 1, Y, \tau) = 0, \quad \frac{\partial c_i}{\partial Y}(X, Y = \pm h/\ell, \tau) = 0, \quad \text{where } i \in [1, 2, 3], \quad (20)$$

where the open end of the pore is located at $X = 0$, impermeable walls are located at $X = 1$ and $Y = \pm h/\ell$, and the aspect ratio is set to $\ell/h = 10$. Outside of the open end of the pore, there is a reservoir of motionless fluid that serves to accept Na^+ and to supply K^+ . The Na^+ ions are initially present only inside of the pore while K^+ is initially present only outside of the pore, i.e., in the reservoir. The Cl^- ions are initially present in equal concentrations inside and outside of the pore.

TABLE I. Nondimensional parameters for computing the solute concentrations c_1 , c_2 , and c_3 and colloidal particle concentration n . The prefactor is $\alpha = \varepsilon k_B^2 T^2 / (e^2 \mu D_1)$, where $\varepsilon = 6.8 \times 10^{-10}$ F/m is the electrical permittivity of the solution, $k_B = 1.38 \times 10^{-23}$ J/K is the Boltzmann constant, $T = 298$ K is the absolute temperature, $e = 1.6 \times 10^{-19}$ C is the elementary charge, and $\mu = 1.0 \times 10^{-3}$ Pa s is the solution viscosity (assumed constant), and $D_1 = 1.33 \times 10^{-9}$ m²/s is the diffusivity of Na⁺ in water [26].

Parameter	Symbol	Value(s) used
Aspect ratio	ℓ/h	10, 20
Maximum initial solute concentration	C_0	1 mM, 10 mM
Valence of Na ⁺	z_1	1
Valence of Cl ⁻	z_2	-1
Valence of K ⁺	z_3	1
Diffusivity of Na ⁺	D_1	1
Diffusivity of Cl ⁻	D_2	1.52
Diffusivity of K ⁺	D_3	1.467
Diffusivity of colloidal particles	D_p	10^{-4} , 10^{-3} , 10^{-2}
Wall reference concentration of Na ⁺	c_{1w}^*	5
Wall reference concentration of Cl ⁻	c_{2w}^*	5
Wall reference concentration of K ⁺	c_{3w}^*	0
Wall reference potential	Ψ_w^*	-4, -2, 0, 2, 4
Particle reference concentration of Na ⁺	c_1^*	5
Particle reference concentration of Cl ⁻	c_2^*	5
Particle reference concentration of K ⁺	c_3^*	0
Particle reference potential	Ψ_p^*	-3
Prefactor	α	0.334

We first present results typical of the time evolution of the cations and anions. Figure 2 shows the results for the aforementioned initial conditions and for $\Psi_w^* = -4$. The color maps shown in Figs. 2(a)–2(c) illustrate the transport of solutes. The steepest gradients are seen at early times (here $\tau = 0.1$), whereas the gradients are smaller already at $\tau = 0.5$ and very weak as the concentration approaches steady state ($\tau = 2.0$). The fluid velocity vector field resulting from the diffusioosmotic wall slip is included on top of each color map. Notably, the X component of each vector field reverses direction near the walls, which is characteristic of a slip-velocity-induced flow field. Figures 2(d)–2(f) show the Y -averaged concentration $\langle c_i \rangle(X, \tau)$ of each ion. From Figs. 2(a)–2(c) we observe that there is no strong variation in the concentration of any of the ions along the Y direction, so the Y -averaged concentration is an accurate representation of the concentration throughout the pore. We see in Fig. 2(d) that Na⁺ tends toward zero concentration at longer times, while we observe in Fig. 2(f) that the K⁺ tends toward the initial concentration of the Na⁺. From Fig. 2(e), we see that the Cl⁻ undergoes a slight increase in concentration from its initial value and then a decrease back. This is an effect that is not present when treating the diffusion of the two solutes NaCl and KCl as independent [35]. In that case, the concentration of Cl⁻ would remain at its initial value.

B. Computing colloidal particle concentration

After evaluating $c_i(X, Y, \tau)$, we calculate the evolution of the colloidal particle concentration n . We considered the case of a particle suspension initially in the pore with no particles in the solution outside the pore. Thus, we take the initial condition

$$n(X, Y, \tau = 0) = 1, \quad (21)$$

and the boundary conditions

$$n(X = 0, Y, \tau) = 0, \quad \frac{\partial n}{\partial X}(X = 1, Y, \tau) = 0, \quad \frac{\partial n}{\partial Y}(X, Y = \pm h/\ell, \tau) = 0, \quad (22)$$

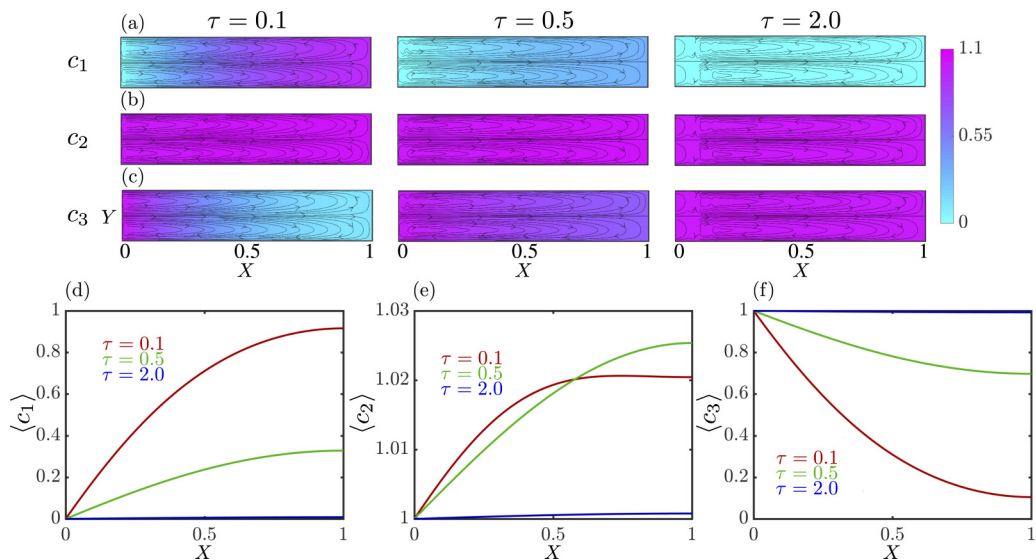


FIG. 2. Simulated codependent diffusion of two solutes, NaCl and KCl, which share a common anion. We consider the three ions Na^+ (c_1), Cl^- (c_2), and K^+ (c_3) diffusing in a finite pore geometry with diffusioosmotic wall slip. Initial and boundary conditions are $c_1(X, Y, \tau = 0) = 1$, $c_2(X, Y, \tau = 0) = 1$, $c_3(X, Y, \tau = 0) = 0$, $c_1(X = 0, Y, \tau) = 0$, $c_2(X = 0, Y, \tau) = 1$, $c_3(X = 0, Y, \tau) = 1$, $\frac{\partial c_i}{\partial X}(X = 1, Y, \tau) = 0$, $\frac{\partial c_i}{\partial Y}(X, Y = \pm h/\ell, \tau) = 0$. (a)–(c) Show the concentration of each respective ion as a color map of the pore at three different times. Each color map also includes a vector plot of the fluid velocity \mathbf{V}_f induced by the diffusioosmotic wall slip. (d)–(f) Show the Y -averaged concentration of each respective ion at the same three times. Note that the vertical axis of (e) spans a much smaller range than the vertical axes of (d) and (f). We use the parameters $\ell/h = 10$, $\Psi_w = -4$, and those identified in Table I.

where the pore geometry and the solute boundary conditions are the same as described in Sec. III A. See the Supplemental Material, movie 1, for an example simulation [33].

Our numerical simulations allow us to calculate the change in the particle distribution in space and time. For example, Fig. 3 shows the particle velocity $\mathbf{V}_p = \mathbf{V}_{\text{DP}} + \mathbf{V}_f$ for a particle diffusivity of $\mathcal{D}_p = 10^{-4}$ and each wall reference potential Ψ_w^* given in Table I. Figures 3(a)–3(e) show the colloidal particle velocity vector field for each respective wall reference potential. As expected, Fig. 3(c), corresponding to zero wall reference potential and therefore to zero wall charge, has no fluid velocity contribution and reduces to a strictly one-dimensional profile. Figures 3(a) and 3(b), which correspond to negative reference wall potentials and therefore to negative wall charge, have a velocity field which diverges from the center line at all times. Figures 3(d) and 3(e), which correspond to positive reference wall potentials and therefore to positive wall charge, have a velocity field which converges toward the center line at the early time and slightly diverges at the two later times. Figures 3(f)–3(j) show the Y -averaged colloidal particle velocity magnitude for each respective reference wall potential at three different times. Notably, the velocity for each value of wall reference potential quickly decays in magnitude such that it is less than half of its value at $\tau = 0.1$ by $\tau = 0.5$. Figures 3(f) and 3(g), which correspond to negative reference wall potentials, are slightly lower in magnitude than Figs. 3(h)–3(j), which have non-negative reference wall potentials. This response is expected, as the leading-order term of the diffusioosmotic slip velocity reverses sign when the wall charge reverses sign, which causes the fluid velocity to subtract less from the diffusiophoretic velocity and possibly add to it.

Next, we explore the consequence of changing the particle diffusivity. Figure 4 shows the colloidal particle concentration for a wall reference potential of $\Psi_w = -4$ and each particle diffusivity \mathcal{D}_p given in Table I. Figures 4(a)–4(c) show the concentration in the pore using a color

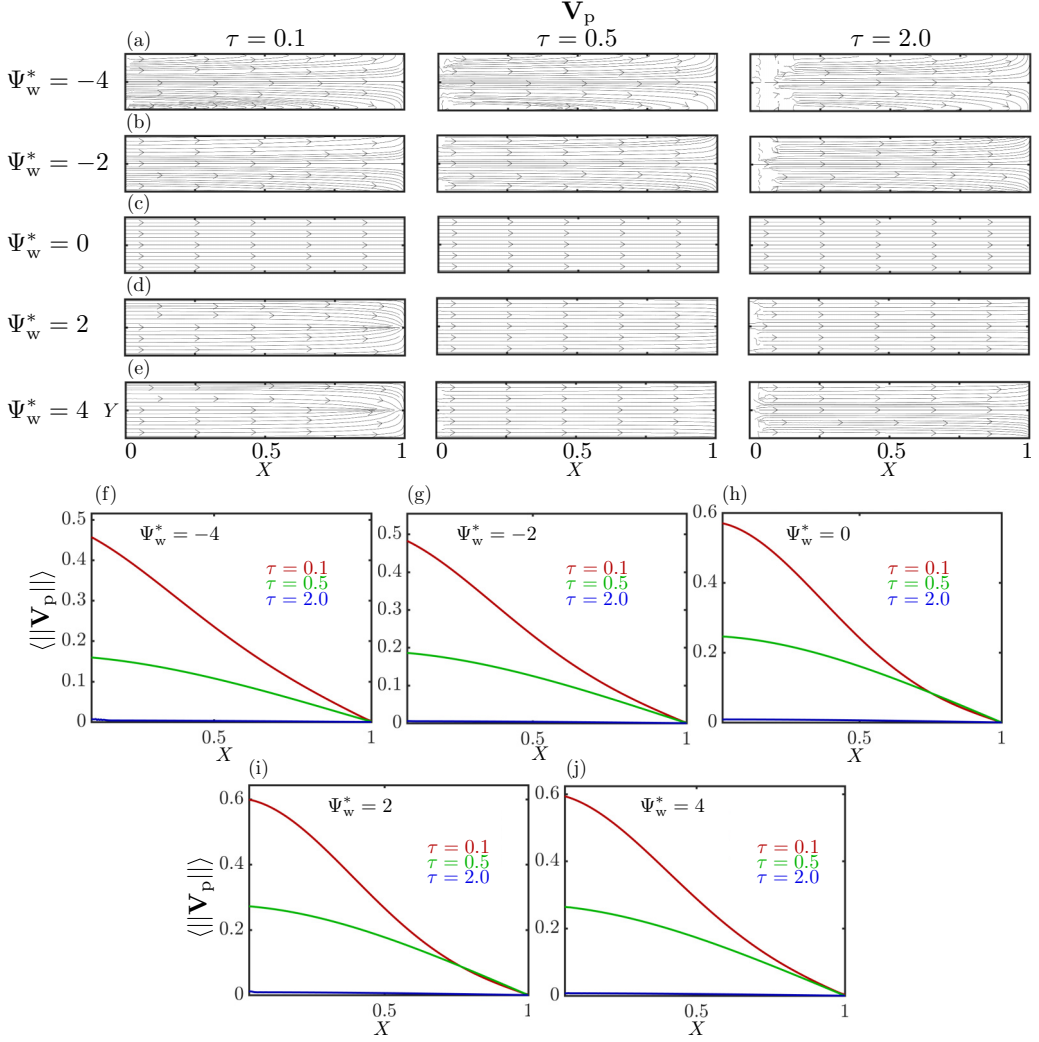


FIG. 3. Simulated colloidal particle velocity \mathbf{V}_p , which is the sum of the diffusiphoretic velocity \mathbf{V}_{DP} and the fluid velocity \mathbf{V}_f . A finite pore geometry is considered with initial condition $n(X, Y, \tau = 0) = 1$ and boundary conditions $n(X = 0, Y, \tau) = 0$, $\frac{\partial n}{\partial X}(X = 1, Y, \tau) = 0$, $\frac{\partial n}{\partial Y}(X, Y = \pm h/\ell, \tau) = 0$. Each wall reference potential given in Table I was simulated. (a)–(e) Show the velocity vector fields. (f)–(j) Show the Y -averaged colloidal particle velocity magnitude $\langle ||\mathbf{V}_p|| \rangle$. Three values of time are used to show the system immediately following the initial conditions, at an intermediate stage, and approaching steady state. We use the parameters $\ell/h = 10$, $D_p = 10^{-4}$, with other values given in Table I.

map. As expected, the contribution of the fluid velocity field decreases as the relative diffusivity increases. The lowest value of relative diffusivity [Fig. 4(a)] results in parabolic contours of the concentration and the highest value [Fig. 4(c)] approaches one-dimensional transport, where the particles diffuse too quickly to be impacted by the two-dimensional fluid velocity. Figures 4(d)–4(f) show the Y -averaged colloidal particle concentration for the three values of particle diffusivity. The concentration reaches higher values of compaction for lower relative diffusivity. Figure 4(d), corresponding to the lowest value of relative diffusivity, has the narrowest peaks in Y -averaged particle concentration. Figure 4(f), corresponding to the highest value of relative diffusivity, has the

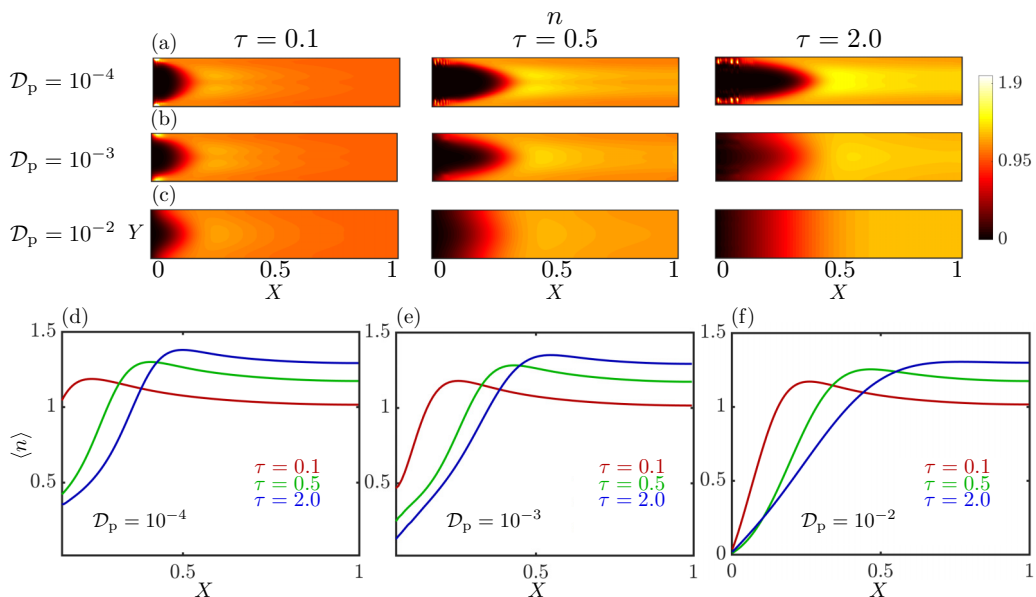


FIG. 4. Simulated colloidal particle concentration n for different particle diffusivities \mathcal{D}_p . A finite pore geometry is considered with initial condition $n(X, Y, \tau = 0) = 1$ and boundary conditions $n(X = 0, Y, \tau) = 0$, $\frac{\partial n}{\partial X}(X = 1, Y, \tau) = 0$, $\frac{\partial n}{\partial Y}(X, Y = \pm h/\ell, \tau) = 0$. The wall reference potential is $\Psi_w^* = -4$. (a)–(c) Show the concentrations for each particle diffusivity in the pore using a color map. (d)–(f) Show the Y -averaged concentrations for each particle diffusivity. Three values of time are used to show the system immediately following the initial conditions, at an intermediate stage, and approaching steady state. We use the parameters $\ell/h = 10$, $\Psi_w = -4$, with other values given in Table I.

broadest peaks. However, the value of the compaction near the dead end of the pore ($X = 1$) is comparable for the three diffusivities.

IV. DEAD-END PORE EXPERIMENTS

In this section we report experiments that we can compare with the numerical results in the preceding section. We use a dead-end pore geometry to perform compaction experiments [34], analogous to the configurations considered in the simulations. Polystyrene (PS; Invitrogen) particles of diameter $1 \mu\text{m}$ are suspended in electrolyte solutions with volume fraction 2.6×10^{-4} . Microfluidic channels are prepared by standard soft lithography and by bonding the PDMS channels to glass slides. The width, height, and length of the main channel and the pores, respectively, are $750 \mu\text{m}$, $150 \mu\text{m}$, and 5cm , and $100 \mu\text{m}$ ($= 2h$), $50 \mu\text{m}$, and 1mm ($= \ell$) [35]. We initially fill the pores with the particle suspension. Then, we introduce an air bubble into the main channel at a volumetric flow rate of $400 \mu\text{L/h}$, which is followed by the second electrolyte solution without particles. Once the two solutions come in contact with each other, the mean flow rate is reduced to $20 \mu\text{L/h}$, corresponding to a mean flow speed $\langle u \rangle = 50 \mu\text{m/s}$ (syringe pump; Harvard Apparatus). Every experiment is repeated three to four times to gain confidence in the quantitative measurements.

The fluorescent images are obtained by using $5\times$ magnification (numerical aperture 0.12) on the inverted microscope (Leica DMI4000B). The depth of field is approximately $60 \mu\text{m}$, which means that, with best focus, the obtained images are two-dimensional projection of the pores, as the pore height is $50 \mu\text{m}$. These image data are suitable for comparison with the numerical simulations. Due to the diffusioosmosis near all walls, such two-dimensional representation of the pores is not identical for different pore heights [36]. For this study, we do not include the details of such

TABLE II. Initial conditions of the solute concentrations for experiments.

Experiment	Main channel	Pore
i	10 mM KCl	2.5 mM NaCl, 7.5 mM KCl
ii	10 mM KCl	5 mM NaCl, 5 mM KCl
iii	10 mM KCl	7.5 mM NaCl, 2.5 mM KCl
iv	10 mM KCl	10 mM NaCl
v	1 mM KCl	1 mM NaCl
vi	5 mM KCl	5 mM NaCl

three-dimensional effects. The chosen geometry allows consistent control of the test parameters, and we obtain clear trends from the experiments listed in Table II.

In order to obtain the two-dimensional intensity data from the experiments, we overlaid five pores ($100 \mu\text{m} \times 1 \text{mm}$) from each experiment using the OR operator from ImageJ. Then the average of three experiments is plotted in the X - Y plane and compared with the results of the numerical simulations. Such image intensity calculations show that the measurements do not perturb the particle mass conservation in the system (Fig. 9). The intensity in each experiment was normalized by the mean gray value at time $\tau = 0$.

Compaction experiments were performed for six different initial conditions of the solutes, as given in Table II. Figures 5–8 compare observed data and simulated data for each of the experimental conditions. The simulations were conducted as described in Sec. III A but with corresponding initial conditions. The parameters were set according to Table II, with aspect ratio $\ell/h = 20$, dimensionless particle diffusivity $\mathcal{D}_p = 10^{-4}$, dimensionless particle reference potential $\Psi_p^* = -3$ [25], and dimensionless wall reference potential $\Psi_w^* = -4$ [25]. The results in Fig. 5 show the simulated and experimental time evolution of the colloid concentration for condition iv from Table II. The experimental data qualitatively match the trends in the simulated data well throughout time, including the parabolic contours due to the diffusioosmotic slip-induced flow field [Figs. 5(a) and 5(b)] but show some quantitative differences [Figs. 5(c) and 5(d)]. For the Y -average and center-line ($Y = 0$) particle concentrations [Figs. 5(c) and 5(d) and later plots], moving averages of periods 40 and 100 are applied, respectively, to reduce the noise in the intensity data. Below we further compare the experiments and simulations for three different sets of conditions to examine different physical effects in the system.

In the first set of experiments, we maintained a concentration of 10 mM KCl in the main channel (i–iv). To examine the effect of multiple ions on diffusio-phoresis of PS particles, we varied the NaCl and KCl concentrations inside the pore such that the total initial electrolyte concentration is also 10 mM (Table II). Effectively, the concentration gradient of KCl is highest for condition iv and lowest for condition i. The comparison between the conditions i–iv and the numerical simulations is shown in Fig. 6. Two-dimensional (2D) profiles of the particle distribution at $\tau = 0.5$ for conditions i–iv [Figs. 6(a)–6(d)] show qualitative agreements between experiments and simulations. Under larger concentration gradients, we observe a larger diffusio-phoretic velocity and consequently a deeper compaction of the particles into the pores. The trend is also observed in the graphs of the Y -averaged and center-line ($Y = 0$) particle concentrations plotted along the pore length [Figs. 6(e) and 6(f)].

We note that the absolute compaction distance of the particles is larger in the experiments as compared to the model. The data in Figs. 6(a)–6(d) suggest that the difference may arise due to the complicated flow structure near the pore inlet. In experiments, there is a flow at finite speed in the main channel, which interacts with advective-diffusive ion transport at the pore inlet. This effect is not captured through the reservoir boundary condition, as assumed in our model. In addition, due to the pressure gradient in the experimental fluid flow, streamlines at the pore inlet are curved and can penetrate into the pore [20], generating a region of mixing that causes smaller diffusioosmotic slip near the pore inlet. In the model calculations, we assume a parabolic velocity profile for the liquid

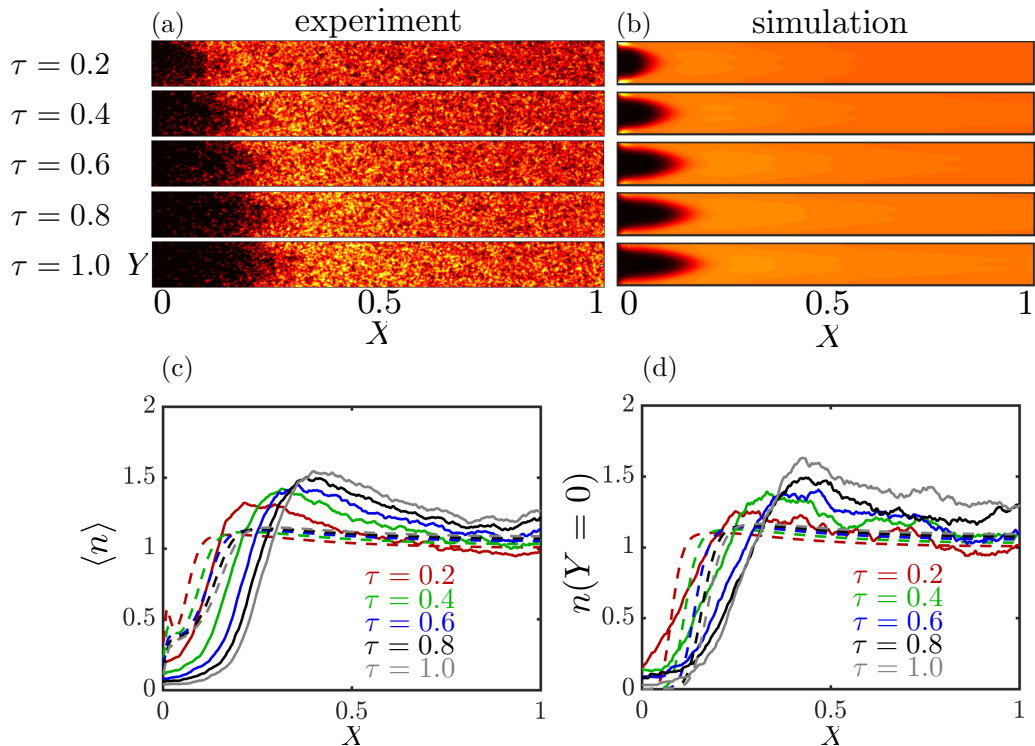


FIG. 5. Comparison between the experimental (solid) and simulated (dashed) time evolution of the colloid concentration for an initial condition of 10 mM KCl in the main channel and 10 mM NaCl in the pore, which is condition iv from Table II. (a) Shows the experimental images of the pore and (b) shows the simulated data at various values of τ . The experimental data qualitatively match the trends in the simulated data well throughout time, including the parabolic contours due to the diffusioosmotic slip-induced flow field [(a) and (b)] but shows some quantitative differences [(c) and (d)]. (c) Shows the Y -averaged colloid concentrations vs X for each value of τ . (d) Shows the center-line ($Y = 0$) colloid concentrations vs X for each value of τ .

flow everywhere and neglect complicating velocity profile effects near the pore inlet. Nevertheless, these effects do not change our analyses of multi-ion diffusiophoresis.

We next demonstrate the effect of the magnitude of the initial solute concentration of KCl and NaCl, as shown in Fig. 7, which compares experimental conditions iv and v. A lower initial concentration of solutes (1 mM), while maintaining the concentration ratios between the solutes, causes an increase in colloid compaction. In order to maintain constant electrical charge, the zeta potential of the colloidal particles and the walls increases in response to the lower electrolyte concentration [Eqs. (8) and (15)]. In the 2D plots [Figs. 7(a) and 7(b)], we observe sharper parabolic profiles with 1-mM electrolytes [Fig. 7(b)]. This is an indication of stronger diffusioosmosis and diffusiophoresis, confirming the effect of increased surface potentials on the wall and the particles. We note that such effect would not have been captured by the numerical simulations if we had assumed a constant zeta potential (on both the particles and the walls).

Next, we compare the conditions ii and vi in order to demonstrate the effect of the background solute (Fig. 8). The condition ii consists of 5 mM KCl in the main channel and 5 mM NaCl in the pores, with an additional background 5 mM KCl in the entire system. Without this background 5 mM KCl, condition vi causes a greater solute gradient, which increases the colloidal compaction. Therefore, the background electrolyte decreases diffusiophoresis. Similar to the results shown in Fig. 7, the sharper parabolic profile in Fig. 8(b) than 8(a) is due to the larger surface potential.

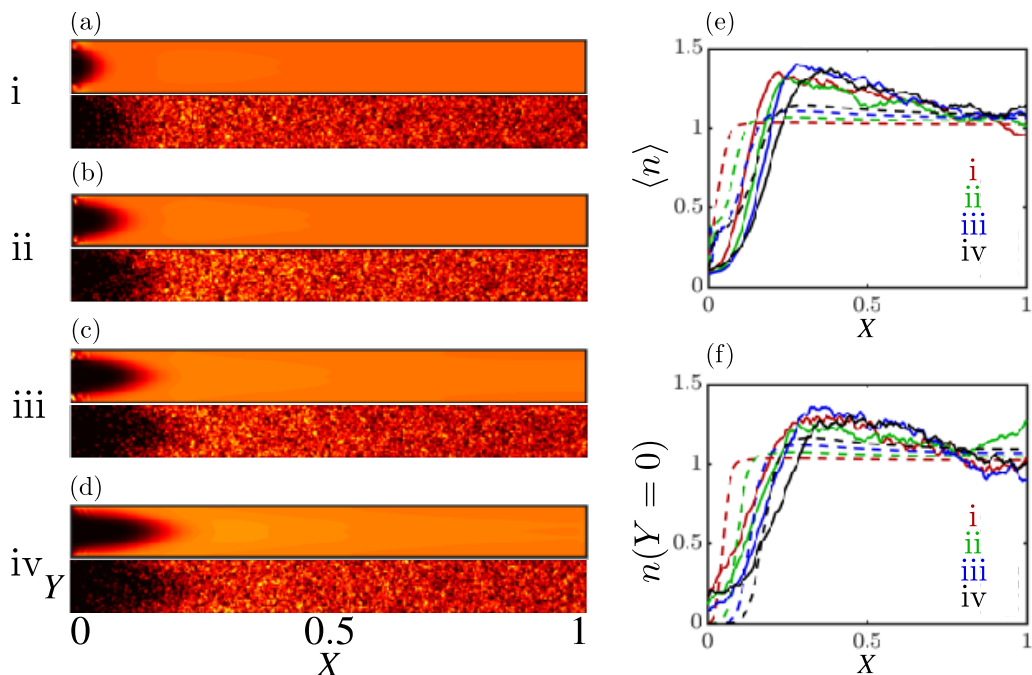


FIG. 6. Comparison between the experiments (solid) and simulations (dashed) for initial conditions of 10 mM KCl in the main channel varying pore concentrations: 2.5 mM NaCl and 7.5 mM KCl, 5 mM NaCl and 5 mM KCl, 7.5 mM NaCl and 2.5 mM KCl, and 10 mM NaCl, which are conditions i–iv from Table II. We note that, for each condition, the total concentration of Cl^- is conserved and the concentrations of Na^+ and K^+ are varied. (a)–(d) Compare the simulated data (top) with experimental images at $\tau = 0.5$. These four experiments demonstrate that creating a larger concentration gradient of KCl increases colloidal compaction. The experimental data qualitatively match the trends in the simulated data well throughout time, including the parabolic contours due to the diffusioosmotic slip-induced flow field [(a)–(d)] but show some quantitative differences [(e) and (f)]. (e) Shows the Y -averaged colloid concentrations versus X for each condition. (f) Shows the center-line ($Y = 0$) colloid concentrations versus X for each condition.

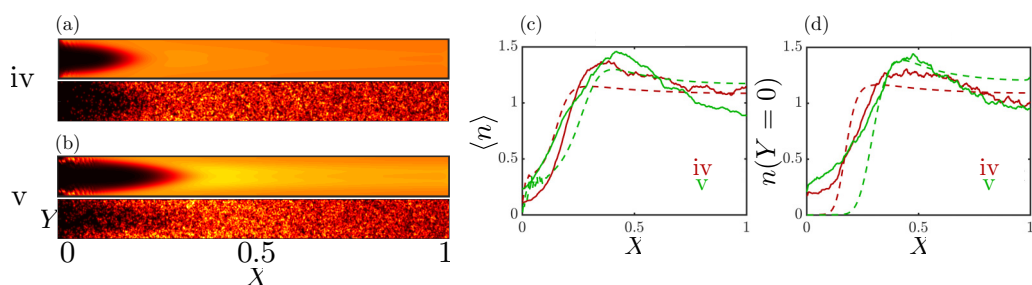


FIG. 7. Comparison between the experiments (solid) and simulations (dashed) for initial conditions of 10 mM KCl in the main channel and 10 mM NaCl in the pore, and 1 mM KCl in the main channel and 1 mM NaCl in the pore, which are conditions iv and v from Table II. The comparison demonstrates the effect of absolute concentration. (a), (b) Compare the simulated pores (top) to the experimental images at $\tau = 0.5$ for conditions iv and v, respectively. We observe deeper colloidal compaction with lower ion concentrations because of a change in the zeta potentials. The experimental data qualitatively match the trends in the simulated data well throughout time, including the parabolic contours due to the diffusioosmotic slip-induced flow field [(a) and (b)] but show some quantitative differences [(c) and (d)]. (c) Shows the Y -averaged colloid concentrations versus X for each condition. (d) Shows the center-line ($Y = 0$) colloid concentrations versus X for each condition.

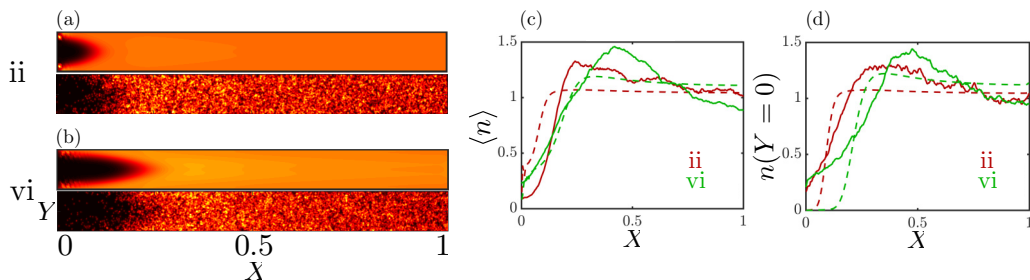


FIG. 8. Comparison between the experiments (solid) and simulations (dashed) for initial conditions of 10 mM KCl in the main channel and 5 mM NaCl and 5 mM KCl in the pore, and 5 mM KCl in the main channel and 5 mM NaCl in the pore, which are conditions ii and vi from Table II. The comparison demonstrates the effect of the background solute. (a), (b) Compare the simulated pores (top) to experimental images at $\tau = 0.5$ for conditions ii and vi, respectively. We see deeper colloid compaction in the absence of background KCl because lower ion concentrations result in larger zeta potentials. The experimental data qualitatively match the trends in the simulated data well throughout time, including the parabolic contours due to the diffusioosmotic slip-induced flow field [(a) and (b)] but show some quantitative differences [(c) and (d)]. (c) Shows the Y -averaged colloid concentrations versus X for each condition. (d) Shows the center-line ($Y = 0$) colloid concentrations versus X for each condition.

The two-dimensional simulations have qualitative agreement with the trends of the experiments. However, quantitative measures including the location of the maximum of the Y -averaged colloid concentration and center-line colloid concentration, the width of the peak of the Y -averaged colloid concentration and center-line colloid concentration, and the magnitude of the colloid concentration cannot be predicted within reasonable accuracy. We observe that the center-line colloid concentrations compare quantitatively better to the experiments than Y -averaged colloid concentrations. This is likely because the pore inlet effects distort the average. In particular, we believe that the singularity in the description of diffusioosmotic velocity yields an unphysically large fluid velocity near the pore inlet, which causes significant colloid transport along the pore walls to the pore inlet, away from the bulk. This would explain the discrepancy for both the center-line colloid concentration and the Y -averaged colloid concentration. In future, we hope to resolve this discrepancy by solving the Navier-Stokes equation for fluid motion near the pore inlet.

V. CONCLUSIONS

In this study, we modeled the time-dependent diffusioophoretic compaction of colloids due to the gradient of a multi-ion solute with a diffusioosmotic slip-driven background flow field. We simulated this system with varying wall and particle properties. This demonstrated that the sign and magnitude of the pore wall charge (Fig. 3) and the magnitude of the particle diffusivity (Fig. 4) can be selected to manipulate the direction and magnitude of the particle velocity by modifying the flow field or the level of interaction between the particles and the flow field. We conducted experiments to determine the effect of the total solute concentrations (Fig. 7) and the presence of a background electrolyte (Fig. 8) and found good qualitative agreement with simulations.

Our results indicate that while the average motion of the particle is governed by the diffusioophoretic process, the dispersion of the particle is dominated by diffusioosmosis; see Fig. 4. In addition, these processes can be tuned by modifying the magnitude and direction of ion gradients; see Figs. 5–8. These findings can be applied, for instance, to improve our understanding of biological processes where charged macromolecules are transported through channels in the presence of ion gradients [37]. Our results on diffusioosmotic background flow may be relevant in energy storage and desalination devices where charge gradients of multiple and multivalent ions are readily present [38–40]. Finally, diffusioophoresis and diffusioosmosis in tandem in multiple ionic gradients are

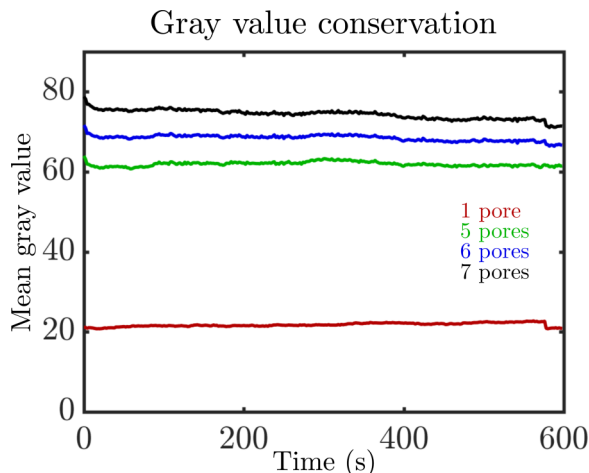


FIG. 9. Mean intensity from the overlaid pore images is plotted versus time. The particle mass conservation in the compaction experiments is maintained after overlaying results from five pores.

important for ion-exchange membranes [41] and colloidal focusing and delivery in lab-on-a-chip applications [15,23].

ACKNOWLEDGMENTS

We thank the High Meadows Environmental Institute at Princeton University for partial support of this research and for supporting summer internships for B.M.A. and E.M.

APPENDIX: PARTICLE MASS CONSERVATION IN EXPERIMENTS

In the image analysis, we overlay five pores from each experiment to obtain continuous particle distribution. In compaction experiments, particle concentration in the pore is conserved over time with little leakage due to the diffusioosmosis. For the fluorescent images obtained under a consistent imaging condition, overlaying five pores did not affect the conservation of the intensity (Fig. 9), which is a measure of particle concentration. Therefore, we use the five-pore-overlaid image as representative data for each experiment.

-
- [1] B. Derjaguin, G. Sidorenkov, E. Zubashchenkov, and E. Kiseleva, Kinetic phenomena in boundary films of liquids, *Kolloidn. zh* **9**, 335 (1947).
 - [2] S. Dukhin, Z. Ul'berg, G. Dvornichenko, and B. Deryagin, Diffusiophoresis in electrolyte solutions and its application to the formation of surface coatings, *Bull. Acad. Sci. USSR, Div. Chem. Sci.* **31**, 1535 (1982).
 - [3] D. Prieve, J. Anderson, J. Ebel, and M. Lowell, Motion of a particle generated by chemical gradients. part 2. electrolytes, *J. Fluid Mech.* **148**, 247 (1984).
 - [4] J. Anderson, M. Lowell, and D. Prieve, Motion of a particle generated by chemical gradients. part 1. non-electrolytes, *J. Fluid Mech.* **117**, 107 (1982).
 - [5] D. C. Prieve, Migration of a colloidal particle in a gradient of electrolyte concentration, *Adv. Colloid Interface Sci.* **16**, 321 (1982).
 - [6] J. L. Anderson and D. C. Prieve, Diffusiophoresis: Migration of colloidal particles in gradients of solute concentration, *Sep. Purif. Methods* **13**, 67 (1984).

- [7] D. C. Prieve and R. Roman, Diffusiophoresis of a rigid sphere through a viscous electrolyte solution, *J. Chem. Soc., Faraday Trans. 2* **83**, 1287 (1987).
- [8] J. L. Anderson, Colloid transport by interfacial forces, *Annu. Rev. Fluid Mech.* **21**, 61 (1989).
- [9] B. Abécassis, C. Cottin-Bizonne, C. Ybert, A. Ajdari, and L. Bocquet, Boosting migration of large particles by solute contrasts, *Nat. Mater.* **7**, 785 (2008).
- [10] J. Palacci, B. Abécassis, C. Cottin-Bizonne, C. Ybert, and L. Bocquet, Colloidal Motility and Pattern Formation under Rectified Diffusiophoresis, *Phys. Rev. Lett.* **104**, 138302 (2010).
- [11] J. Palacci, S. Sacanna, A. P. Steinberg, D. J. Pine, and P. M. Chaikin, Living crystals of light-activated colloidal surfers, *Science* **339**, 936 (2013).
- [12] J. T. Ault, S. Shin, and H. A. Stone, Diffusiophoresis in narrow channel flows, *J. Fluid Mech.* **854**, 420 (2018).
- [13] A. Gupta, S. Shim, and H. A. Stone, Diffusiophoresis: From dilute to concentrated electrolytes, *Soft Matter* **16**, 6975 (2020).
- [14] D. C. Prieve, S. M. Malone, A. S. Khair, R. F. Stout, and M. Y. Kanj, Diffusiophoresis of charged colloidal particles in the limit of very high salinity, *Proc. Natl. Acad. Sci. USA* **116**, 18257 (2019).
- [15] A. Banerjee, I. Williams, R. N. Azevedo, M. E. Helgeson, and T. M. Squires, Solute-inertial phenomena: Designing long-range, long-lasting, surface-specific interactions in suspensions, *Proc. Natl. Acad. Sci. USA* **113**, 8612 (2016).
- [16] A. Kar, T.-Y. Chiang, I. Ortiz Rivera, A. Sen, and D. Velegol, Enhanced transport into and out of dead-end pores, *ACS Nano* **9**, 746 (2015).
- [17] S. Shin, E. Um, B. Sabass, J. T. Ault, M. Rahimi, P. B. Warren, and H. A. Stone, Size-dependent control of colloid transport via solute gradients in dead-end channels, *Proc. Natl. Acad. Sci. USA* **113**, 257 (2016).
- [18] J. T. Ault, P. B. Warren, S. Shin, and H. A. Stone, Diffusiophoresis in one-dimensional solute gradients, *Soft Matter* **13**, 9015 (2017).
- [19] S. V. Hartman, B. Božič, and J. Derganc, Migration of blood cells and phospholipid vesicles induced by concentration gradients in microcavities, *New Biotechnology* **47**, 60 (2018).
- [20] S. Battat, J. T. Ault, S. Shin, S. Khodaparast, and H. A. Stone, Particle entrainment in dead-end pores by diffusiophoresis, *Soft Matter* **15**, 3879 (2019).
- [21] N. Singh, G. T. Vladislavjević, F. Nadal, C. Cottin-Bizonne, C. Pirat, and G. Bolognesi, Reversible Trapping of Colloids in Microgrooved Channels via Steady-State Solute Gradients, *Phys. Rev. Lett.* **125**, 248002 (2020).
- [22] T.-Y. Chiang and D. Velegol, Multi-ion diffusiophoresis, *J. Colloid Interface Sci.* **424**, 120 (2014).
- [23] N. Shi, R. Nery-Azevedo, A. I. Abdel-Fattah, and T. M. Squires, Diffusiophoretic Focusing of Suspended Colloids, *Phys. Rev. Lett.* **117**, 258001 (2016).
- [24] M. Seo, S. Park, D. Lee, H. Lee, and S. J. Kim, Continuous and spontaneous nanoparticle separation by diffusiophoresis, *Lab Chip* **20**, 4118 (2020).
- [25] S. Shin, J. T. Ault, J. Feng, P. B. Warren, and H. A. Stone, Low-cost zeta potentiometry using solute gradients, *Adv. Mater.* **29**, 1701516 (2017).
- [26] D. Velegol, A. Garg, R. Guha, A. Kar, and M. Kumar, Origins of concentration gradients for diffusiophoresis, *Soft Matter* **12**, 4686 (2016).
- [27] W. M. Deen, *Analysis of Transport Phenomena* (Oxford University Press, Oxford, 2012).
- [28] H. J. Keh and H. C. Ma, Diffusioosmosis of electrolyte solutions along a charged plane wall, *Langmuir* **21**, 5461 (2005).
- [29] A. Gupta, B. Rallabandi, and H. A. Stone, Diffusiophoretic and diffusioosmotic velocities for mixtures of valence-asymmetric electrolytes, *Phys. Rev. Fluids* **4**, 043702 (2019).
- [30] T. W. Healy and L. R. White, Ionizable surface group models of aqueous interfaces, *Adv. Colloid Interface Sci.* **9**, 303 (1978).
- [31] L. D. Landau and E. M. Lifshitz, *Fluid Mechanics, Second Edition: Volume 6 (Course of Theoretical Physics)* (Butterworth-Heinemann, Oxford, 1987).
- [32] MATLAB version 9.3.0.713579 (R2017b) (The Mathworks, Inc., Natick, Massachusetts, 2017).
- [33] See Supplemental Material at <http://link.aps.org/supplemental/10.1103/PhysRevFluids.6.054201> for movie 1.

- [34] J. L. Wilson, S. Shim, Y. E. Yu, A. Gupta, and H. A. Stone, Diffusiophoresis in multivalent electrolytes, [Langmuir](#) **36**, 7014 (2020).
- [35] A. Gupta, S. Shim, L. Issah, C. McKenzie, and H. A. Stone, Diffusion of multiple electrolytes cannot be treated independently: Model predictions with experimental validation, [Soft Matter](#) **15**, 9965 (2019).
- [36] J. T. Ault, S. Shin, and H. A. Stone, Characterization of surface-solute interactions by diffusioosmosis, [Soft Matter](#) **15**, 1582 (2019).
- [37] G. Bruno, N. Di Trani, R. L. Hood, E. Zabre, C. S. Filgueira, G. Canavese, P. Jain, Z. Smith, D. Demarchi, S. Hosali *et al.*, Unexpected behaviors in molecular transport through size-controlled nanochannels down to the ultra-nanoscale, [Nat. Commun.](#) **9**, 1682 (2018).
- [38] A. Gupta, A. Govind Rajan, E. A. Carter, and H. A. Stone, Ionic Layering and Overcharging in Electrical Double Layers in a Poisson-Boltzmann Model, [Phys. Rev. Lett.](#) **125**, 188004 (2020).
- [39] A. Gupta, P. J. Zuk, and H. A. Stone, Charging Dynamics of Overlapping Double Layers in a Cylindrical Nanopore, [Phys. Rev. Lett.](#) **125**, 076001 (2020).
- [40] S. E. Bone, H.-G. Steinrück, and M. F. Toney, Advanced characterization in clean water technologies, [Joule](#) **4**, 1637 (2020).
- [41] D. Florea, S. Musa, J. M. Huyghe, and H. M. Wyss, Long-range repulsion of colloids driven by ion exchange and diffusiophoresis, [Proc. Natl. Acad. Sci. USA](#) **111**, 6554 (2014).